

WIRELESSLY POWERED HIGH-TEMPERATURE STRAIN MEASURING PROBE BASED ON PIEZORESISTIVE NANOCRYSTALLINE DIAMOND LAYERS

Adam Bouřa, Pavel Kulha, Miroslav Husák

*Czech Technical University in Prague, Department of Microelectronics, Technická 2, 166 27 Prague 6, Czech Republic
(✉ bouraa@fel.cvut.cz, +420 224 352 335, kulhap@fel.cvut.cz, husak@fel.cvut.cz)*

Abstract

A high-temperature piezo-resistive nano-crystalline diamond strain sensor and wireless powering are presented in this paper. High-temperature sensors and electronic devices are required in harsh environments where the use of conventional electronic circuits is impractical or impossible. Piezo-resistive sensors based on nano-crystalline diamond layers were successfully designed, fabricated and tested. The fabricated sensors are able to operate at temperatures of up to 250°C with a reasonable sensitivity. The basic principles and applicability of wireless powering using the near magnetic field are also presented. The system is intended mainly for circuits demanding energy consumption, such as resistive sensors or devices that consist of discrete components. The paper is focused on the practical aspect and implementation of the wireless powering. The presented equations enable to fit the frequency to the optimal range and to maximize the energy and voltage transfer with respect to the coils' properties, expected load and given geometry. The developed system uses both high-temperature active devices based on CMOS-SOI technology and strain sensors which can be wirelessly powered from a distance of up to several centimetres with the power consumption reaching hundreds of milliwatts at 200°C. The theoretical calculations are based on the general circuit theory and were performed in the software package Maple. The results were simulated in the Spice software and verified on a real sample of the measuring probe.

Keywords: nano-crystalline diamond, strain sensor, high temperature, remote sensing, wireless powering.

© 2016 Polish Academy of Sciences. All rights reserved

1. Introduction

1.1. General considerations

Electronic devices and sensors for diagnostic and control systems are required to operate at ever increasing temperatures. Standard commercial bulk silicon processes are unable to deal with these demanding requirements. The application of standard components above their intended range is neither recommended nor specified by their manufacturers. Operation of devices at temperatures greater than 200°C is required for a variety of current as well as next-generation control systems including industrial, automotive, aircraft and aerospace applications. It is required to design special components specified for operation in the harsh (high-temperature) environment. There are several suitable semiconductor technologies for high-temperature and harsh-environment applications, such as SOI, GaAs, SiC, GaN, AlN, and diamond [1]. Generally, high-temperature usability of silicon devices is limited (up to ~300°C), but for some applications this technology is still suitable, because it is well established and its maturity is very high. The future of high-temperature electronic devices lies probably in wide-bandgap semiconductors such as silicon carbide, semiconductors from the III-nitrides family (e.g. GaN, AlN), or diamond [2].

1.2. Nano-crystalline diamond based sensors

The unique combination of material properties of diamond, such as its physical hardness, high Young's modulus, low coefficient of friction, chemical inertness and high thermal conductivity, are ideal for such applications as force sensors, pressure sensors, accelerometers, and other strain-related sensors [3]. Furthermore, crystalline diamond films are bio-compatible and – along with their piezo-resistive nature – are very suitable for biosensors [4], radiofrequency applications and power electronics [5].

1.3. Wireless powering

The wireless powering is suitable in situations where the standard powering cannot be applied. The battery powering is used when the powering wires cannot be attached to a sensor (*e.g.* in a rotating device). Unfortunately, this is not suitable for every application. The main disadvantage of the battery powering is a limited lifetime of devices (biomedical probes, sensors embedded in concrete walls, *etc.*) and the environments (especially high-temperature ones) unsuitable for the batteries. Energy harvesting can be used to overcome the limited lifetime of batteries [6], but usually they are still not suitable to use in harsh environments. In those cases, the wireless powering is advantageous.

The wireless powering based on the near magnetic field is a relatively mature technology and it is widely used in such applications, as passive *Radiofrequency Identification* (RFID) systems [7]. Unfortunately, the power consumption of a passive RFID tag is usually small. Thus, standard RFID circuits cannot be used for power demanding applications. One example of power demanding application is the battery charging [8, 9]. A disadvantage of this solution is the complexity of the powering circuit. It is usually based on an application-specific integrated circuit (*e.g.* [10]). Moreover, the circuit must be operated only under defined conditions – namely the operating temperature.

The powering using the near magnetic field is a hot topic in different applications that are not covered by the above mentioned matured technologies and research is still in progress. There are high-power applications which are usually used in automotive industry and that are capable of transferring several kilowatts [11]. The *Wireless Power Transfer* (WPT) in low power applications is focused mainly on biomedical implants [12], small device charging [8] and general remote probes.

1.4. Applications for wireless and high-temperature monitoring

Wireless systems are successfully used in industrial applications, such as the structural health monitoring, stress measurement and fatigue analysis. The system presented in the paper is intended to use for monitoring the stress of blade in an industrial steam turbine. The methods of structural health monitoring cover contactless tip-timing techniques using blade-tip vibrometers based on capacitive [13], magneto-resistive [14] or optical sensors [15], as well as contact techniques using fibre grating sensors [16] or mostly used strain gauges [17]. The latter method enables to monitor blade fatigue failures by studying the characteristic of flow-induced resonant vibration. The natural frequency is altered by the presence of a crack in a turbine blade. On-rotor operation of the blade mounted sensors may face some challenges as the strain gauge device may fail due to the high temperature and aggressive environment in the gas turbine [18]. The developed system presented in the paper reduces some weaknesses of common systems using high-temperature strain gauges together with the wireless powering, which can extend the lifetime and improve effective operation inside turbine.

2. High temperature strain sensor

2.1. Piezo-resistive effect in nano-crystalline diamond

Piezo-resistive properties of diamond polycrystalline film were firstly quantified by Aslam *et al.* [19]. Since then, piezo-resistive properties have been studied by several research groups and the *Gauge Factor* (GF) was observed to be in the range from $GF = 2$ to $GF = 4000$ [20, 21]. However, a clear explanation of the piezo-resistive behaviour and the dependence of GF on temperature and impurity concentration have not yet been presented. Diamond layers usually used in piezo-resistive sensors have mostly a poly- or nano- crystalline structure. Polycrystalline materials consist of small single crystalline grains interconnected by grain boundaries. The grain boundaries have a significant influence on the material properties. Defects on the grain boundaries create trapping states and/or segregation sites. The GF (–) can be generally expressed as a fractional change in resistivity ρ ($\Omega \cdot m$) per mechanical strain ε (–) by the (1):

$$GF = \frac{\Delta\rho}{\rho} \cdot \frac{1}{\varepsilon}. \quad (1)$$

The crystal structure, effects on grain boundaries, resistivity, and thus GF are influenced by many technological aspects, such as the method of growth, temperature, pressure, and mainly the doping level (given by the boron to carbon ratio during the layer growth) which is discussed in this paper.

2.2. FEM modelling

Modelling and simulation of mechanical stresses and deformations is virtually essential for any design of micro-sensor structures. The mechanical and piezo-resistive simulations were performed with the software Coventor package using MemMech and MemPZR solver. The FEM simulations were used to estimate the sensor sensitivity, to optimize the sensor position on the substrate with respect to the high stress areas – to estimate the sensitivity variations (by changing its offset), and to simulate the temperature dependence on the deformation sensitivity.

The single resistor structures with a constant length (Fig. 1a) and a constant width (Fig. 1b) were designed for testing the fabrication technology and estimating the basic parameters (piezo-resistors with lengths from 500 μm to 2000 μm and widths from 25 μm to 200 μm).

Simulating the optimum sensor position on the substrate was simplified and performed on a single side-fixed cantilever beam loaded at the free end by a force of 0.4 N. Full-bridge structures were designed for real applications, as shown in Fig. 2b. Four meander-like piezo-resistors are connected to form full-bridges of 450 μm , or a 675 μm meander edge.

Piezo-resistors are sensitive to the offset with respect to the point of fixing, as shown in Fig. 1. The simulation showed that piezo-resistors with a constant length are less sensitive to the offset than the piezo-resistors with a constant width (Fig. 1c, 1d). The centre of resistor with $L = 2$ mm should be placed 0.2 mm from the point of fixing, while that of resistor with $L = 1.5$ mm should be placed 1 mm from the point of fixing, as shown in Fig. 1d. The longer resistor has also a slightly lower sensitivity (11%). The simulated average stress in a U-shaped piezo-resistor of 1000 μm length and 200 μm width is $\bar{\sigma}_{AV} = 112$ MPa, and the relative strain is $\varepsilon = 1.24 \cdot 10^{-4}$ (–). The temperature dependence of GF was simulated for the temperature range of up to 250°C. GF decreases with increasing the temperature in agreement with [22, 23] to the values of $GF = 2.5$ (–), 8.4 (–) and 4.6 (–) with respect to the B:C concentrations of 500 ppm, 3000 ppm and 6000 ppm, respectively, as shown later in Fig. 6b.

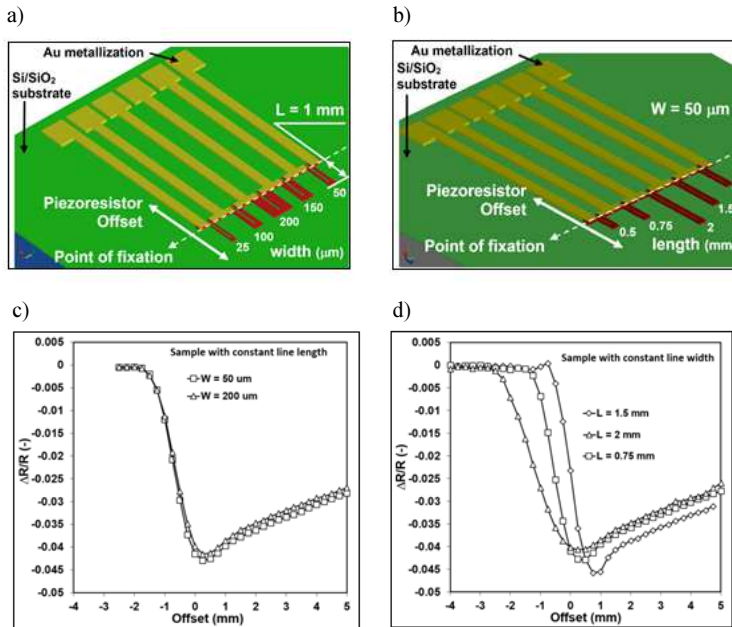


Fig. 1. FEM models of single piezo-resistive structures with: a) a constant length; b) single resistor piezo-resistive structures with a constant width; c) the analysis results for single resistors with a constant length ($L = 1$ mm); d) with a constant width ($W = 50$ μm).

2.3. Sensor fabrication

The piezo-resistive sensing boron-doped diamond thin films were deposited on $\text{SiO}_2/\text{Si}_3\text{N}_4/\text{Si}$ substrates of size 8×25 mm^2 . Substrates were cleaned and seeded in ultrasonic bath. The boron-doped films were grown in an ASTeX 6500 system at the following process parameters: gas pressure 50 torr, microwave power 4000 W, 2% of methane diluted in hydrogen, growth time 30 minutes. The boron doping was achieved by adding *Trimethylboron* (TMB) to the gas mixture and the B:C ratio was 500, 3000 or 6000 ppm in the gas phase. After the deposition, all samples were lithographically processed and the piezo-resistive structures were formed by reactive ion etching in an O_2/CF_4 gas mixture. The thickness of diamond film was 250 ~ 300 nm. The size of diamond crystals was 100 – 200 nm.

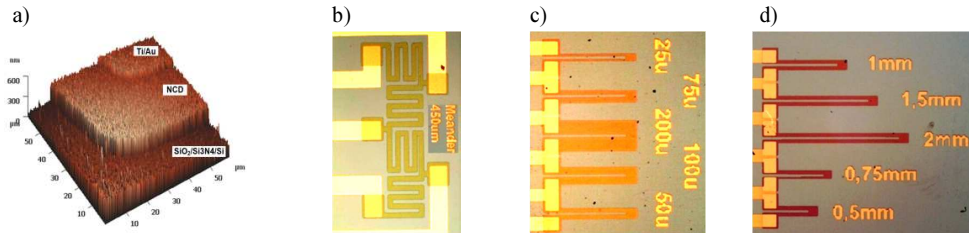


Fig. 2. Morphology of the nano-crystalline diamond layer: a) the AFM image with a detail of piezo-resistive film with Ti/Au contact; b) an image of the full bridge structure with the 450 $\mu\text{m} \times 450$ μm meander; c) the set of resistors with a constant length of 1 mm; d) a constant width of 50 μm .

Finally, Ti and Au thin films (100 nm/100 nm) were evaporated on piezo-resistive structures to form metal contacts with thickness of 90 nm. The detailed procedure of the technological

process can be found in [24]. The ball bonding technique was used to connect Ti/Au contact pads to a gold-plated terminal board.

3. Model of inductive powering

3.1. Basic equations

Figure 3a shows a basic scheme of the inductive powering. The voltage source V_0 is the excitation voltage, R_0 represents the internal resistivity of excitation voltage source, the resistors R_{L1} , R_{L2} represent the parasitic resistivity of inductors L_1 , L_2 , and the resistor R_L is the load where the power should be delivered. The capacitors C_1 and C_2 are added in the circuit to cause a resonant behaviour which maximizes the voltage transfer.

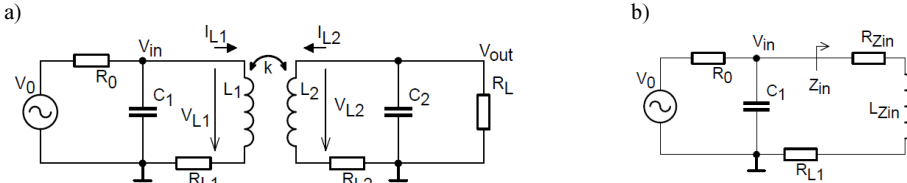


Fig. 3. a) A basic scheme of the inductive powering; b) the input part of inductive powering scheme with the equivalent model of input impedance Z_{in} .

The inductive coupling in the circuit can be described using the equations that relate the voltage phasors V_{L1} , V_{L2} , current phasors I_{L1} , I_{L2} and loading impedance Z_L to the angular frequency $j\omega$ according to the figure. The impedance Z_L represents a combination of components C_2 , R_{L2} , R_L . The coupling between the inductors is characterized by the coupling coefficient k . The coefficient characterizes the geometry of coils and in some specific cases it is not dependent on the number of turns (e.g. if tightly wound solenoid coils are used) [25]. The equations can be used for derivation of the basic relations in the circuit [26].

The most important parameter is the voltage transfer which is given by (2). Another important parameter is the input impedance which can be seen on the inductor L_1 (3):

$$\hat{V}_{L2} = \hat{V}_{L1} \cdot \frac{k \cdot \hat{Z}_L \cdot \sqrt{\frac{L_2}{L_1}}}{\hat{Z}_L + j\omega L_2 \cdot (1 - k^2)}, \quad (2)$$

$$\hat{Z}_{in} = \frac{\hat{V}_{L1}}{\hat{I}_{L1}} = \frac{j\omega L_1 \cdot \hat{Z}_L + j\omega L_1 \cdot j\omega L_2 \cdot (1 - k^2)}{\hat{Z}_L + j\omega L_2}, \quad (3)$$

$$\hat{Z}_L = \frac{R_L + R_{L2} + j\omega C_2 \cdot R_L \cdot R_{L2}}{j\omega C_2 \cdot R_L + 1}. \quad (4)$$

This impedance depends on the loading impedance Z_L and the coupling coefficient k . Transformation of Z_L to the primary side is significant especially in resonance and it can be used for the data transfer from the remote probe [27]. According to Fig. 3a, the loading impedance consists of the loading resistance R_L , parasitic resistance R_{L2} and capacitor C_2 . It can be calculated using (4). The resistor R_L stands for the powered device. The capacitor C_2 is keeping the secondary side in resonance and it is a crucial part of the powering strategy, because the voltage transfer is then maximal.

3.2. Resonance behaviour of circuit

It is evident from Fig. 3a, that the circuit exhibits some resonant behaviour. Combining (2) and (4), the voltage transfer can be derived. Its value is maximal in the resonance. Fig. 4a presents the Spice simulation result of the circuit for given components. The resonance is characterized by a discontinuous change of the voltage transfer phase (the dotted curve in the figure). It means that the real part of the transfer is null. The resonance frequency can be derived by separating the real part from the voltage transfer and solving it for zero. The resonance angular frequency is then given by (5). The resonance frequency depends on the secondary side components and it can be easily tuned using the capacitor C_2 . The absolute value of voltage transfer in the resonance is given by the imaginary part of general voltage transfer and it can be calculated using (6).

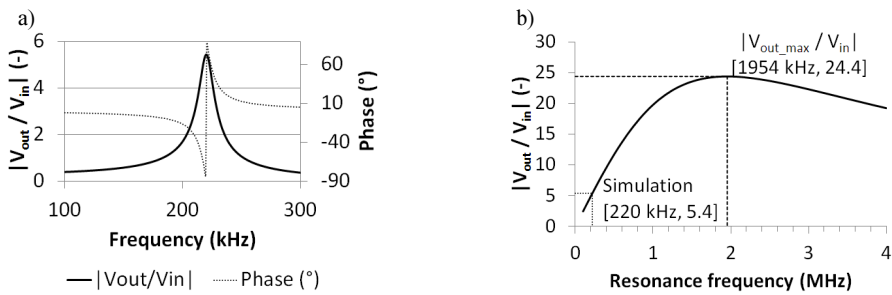


Fig. 4. a) The simulation result of the voltage transfer according to Fig. 3a ($L_1 = 5.4 \mu\text{H}$, $L_2 = 52.7 \mu\text{H}$, $R_{L2} = 4.1 \Omega$, $R_L = 100 \text{k}\Omega$, $k = 0.1$, $V_0 \approx V_{in} = 1 \text{V}$, $R_0 = R_{L1} = 0 \Omega$, $C_1 = 0 \text{F}$, $C_2 = 10 \text{nF}$);
 b) the calculated functional dependency of the voltage transfer in the resonance on the resonance frequency for the same circuit (C_2 sets the circuit in the resonance).

$$\omega_{res} = \frac{R_L + R_{L2}}{R_L \cdot \sqrt{L_2 \cdot C_2 \cdot (1 - k^2)} - R_{L2}^2 \cdot C_2^2}, \quad (5)$$

$$\left| \frac{\hat{V}_{out_res}}{\hat{V}_{in}} \right| = \frac{k \cdot R_L \cdot \sqrt{\frac{L_2}{L_1}} \cdot \sqrt{L_2 \cdot C_2 \cdot (1 - k^2)} - R_{L2}^2 \cdot C_2^2}{R_L \cdot R_{L2} \cdot C_2 + L_2 \cdot (1 - k^2)}. \quad (6)$$

Figure 4b presents the functional dependency of the voltage transfer in the resonance on the resonance frequency. For the given components the resonance is set using the capacitor C_2 . To obtain the functional dependency, the capacitor C_2 value was expressed for the required resonance angular frequency ω_{res} from (5). This expression was substituted into (6). The function is too complex to be presented here. Therefore, only its graphical representation is shown in Fig. 4b.

It is evident from this chart that there exists an optimal resonance frequency maximizing the voltage transfer for the given coils and loading impedance. Two important points are marked in the chart. The dashed lines mark the maximal voltage transfer for the resonance frequency of 1.954 MHz ($C_2 = 127 \text{pF}$) and the dotted lines correspond to the resonance frequency according to Fig. 4a.

3.3. Optimal resonance frequency

The optimal resonance frequency can be found by differentiating the equation that is represented by the curve in the Fig. 4b and solving it for zero. It is given by (7). This equation relates only to the resistors, secondary inductance and the coupling coefficient. The optimal resonance is achieved using the capacitor C_2 and it can be found from (5) and (7). The capacitor C_2 value for the optimal resonance frequency is given by (8). The maximal voltage transfer for the optimal resonance frequency can be calculated combining the (6) and (8). Its value is given by (9) and it is in accordance with the dashed lines marked in Fig. 4b:

$$f_{res_opt} = \frac{1}{2 \cdot \pi} \cdot \frac{(R_L + 2 \cdot R_{L2}) \cdot \sqrt{R_L \cdot R_{L2} + R_{L2}^2}}{R_L \cdot L_2 \cdot (1 - k^2)}, \quad (7)$$

$$C_{2_opt} = \frac{L_2 \cdot (1 - k^2)}{R_{L2} \cdot (R_L + 2 \cdot R_{L2})}, \quad (8)$$

$$\left| \frac{\hat{V}_{out_max}}{\hat{V}_{in}} \right| = \frac{R_L \cdot k \cdot \sqrt{\frac{L_2}{L_1}}}{2 \cdot \sqrt{R_{L2} \cdot (R_L + R_{L2})}}. \quad (9)$$

3.4. Input impedance behaviour

When the resonance is present, the scheme from Fig. 3a can be reduced to the equivalent circuit for the input impedance Z_{in} . The input impedance has the resistive part R_{Zin} and the inductive part L_{Zin} (see Fig. 3b). The equations that describe the input impedance are generally very complex but they can be simplified for the special case of the optimal resonance. They can be further simplified for small values of the coupling coefficient and loaded output ($R_L \ll \infty$), because in this case the parameter k^4 can be neglected. For the optimal resonance frequency f_{res_opt} according to (7) the real and imaginary parts of the input impedance Z_{in_opt} can be assigned to the reactance of the equivalent resistor and inductor according to (10):

$$\hat{Z}_{in_opt} \approx \frac{k^2 L_1}{L_2} \cdot \left(\frac{R_L}{2} + R_{L2} \right) + j\omega L_1 \cdot (1 - k^2). \quad (10)$$

Knowing the input impedance, a parallel resonance can be set also on the primary side using the capacitor C_1 . The resulting resonance tank circuit has a high impedance and the reactive current of the source is reduced. The impedance of the circuit is very sensitive to the loading impedance change which can be used for the passive signal transfer [27]. This method is widely used in passive RFID systems.

3.5. Influence of omitted parasitic parameters

Figure 3b presents the primary side of powering circuit for the optimal resonance frequency. The coupled coils and the load are replaced by the equivalent impedance. In the scheme, an influence of the parasitic resistances R_{L1} and R_0 on the voltage transfer is evident. The input voltage is reduced by the voltage drop on these parasitic resistances. This voltage drop must be compensated by increasing the voltage V_0 to obtain the voltage transfer according to (9). The resonance frequency shift caused by these resistors is usually negligible when high quality coils are used. The coils' inductivity can be also usually presumed to be constant (not frequency-dependent).

The equations were derived for the ideal capacitor C_2 . In a real application the losses in this capacitor can influence the resonance frequency and the voltage transfer. The dissipation factor of the capacitor can be modelled using a parallel resistor that can be included in the loading resistor R_L .



3.6. Coupling coefficient

The coupling coefficient value is a crucial parameter for the powering capability prediction. It characterizes the configuration and geometry of the powering coils and surrounding environment. It can be measured and derived from the voltage transfer (2). The measurement must be performed for the unloaded output ($Z_L \rightarrow \infty$) and for a frequency much lower than the resonant frequency of the secondary side. In compliance with these rules, the coupling coefficient is given by (11):

$$\lim_{Z_L \rightarrow \infty} \hat{V}_{L2} = \hat{V}_{L1} \cdot k \cdot \sqrt{\frac{L_2}{L_1}} \Rightarrow k = \frac{\hat{V}_{L2}}{\hat{V}_{L1}} \cdot \sqrt{\frac{L_1}{L_2}} \quad (11)$$

When tightly wound solenoid coils are used, the coupling coefficient is independent of the number of turns [25] and it characterizes the overall configuration of the coils. In this case, knowing the coefficient's character can be used for predicting its value for arbitrary coils of similar shape and configuration.

Table 1. The coils used in experiments.

Picture		
Label	Primary	Secondary
Diameter (mm)	120	30
Winding number (loops)	11	30
Inductivity (μH)	28.6	60.6*; 57.8**; 49.1***
Serial resistivity (Ω)	0.4	3.5
Self-resonance frequency (MHz)	9.7	5.3
Wire diameter (mm)	0.6	0.15
* Coil in free space ** Large metal plate over the coil in distance 13 mm *** Large metal plate over the coil in distance 3 mm		

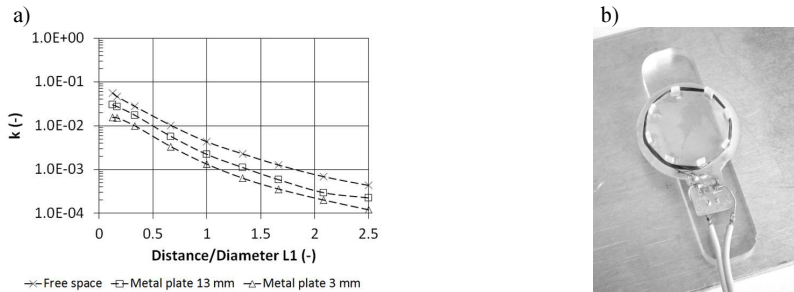


Fig. 5. The axial distance dependency of the coupling coefficient between the coils. The coil L_1 (120 mm diameter) is considered as the primary winding. a) The secondary coil (30 mm diameter) is measured in the free space or with a parallel metal plate below the coil in the distances of 3 mm and 13 mm (the metal plate is on the outer side – not between the coils); b) the secondary coil above the large metal plate in the distance defined by the ceramic pad.

Table 1 presents the coils that have been used in experiments. The secondary coil's inductivity is affected by the presence of a metal plate that is perpendicular to the coil's axis and situated in a defined position (see Fig. 5b). The metal plate simulates a real situation for wireless powering mounted on the metal blade.

Figure 5a shows the measurement results of the coupling coefficient for different axial distances between the coils and different positions of the metal plate. As the primary winding a 120 mm diameter coil with 11 loops is used. The secondary coil was tested in the free space or with a large metal plate placed in the parallel plane below the coil and fixed in a specific position using a ceramic pad. The presence of the metal plate significantly decreases the coupling coefficient value and it is lowering the coil's inductivity. The ratios of the distance between the coils and the primary coil diameter are presented in Fig. 5a. The curves are thus valid for all circular coils with similar ratios of diameters.

4. Measurement results

4.1. High-temperature sensor

An extensive study of sensor parameters, e.g. the deformation sensitivity, the *Temperature Dependences of Resistance* (TCR) and *GF*, and the bridge output voltage under loading, was performed. The measurement results exhibit a reasonable deformation sensitivity of the diamond strain gauges ($GF = 12.8, 12.1$ and 7.6 (-)) and the temperature dependence of resistance ($TCR = 2400, 1150$ and 270 ppm/K) reflecting the doping level (500, 3000 and 6000 ppm, respectively) of the boron to carbon ratio in the gas phase. The system was tested under different temperature loading up to $\sim 250^\circ\text{C}$. The representative measurement results are shown in Fig. 6.

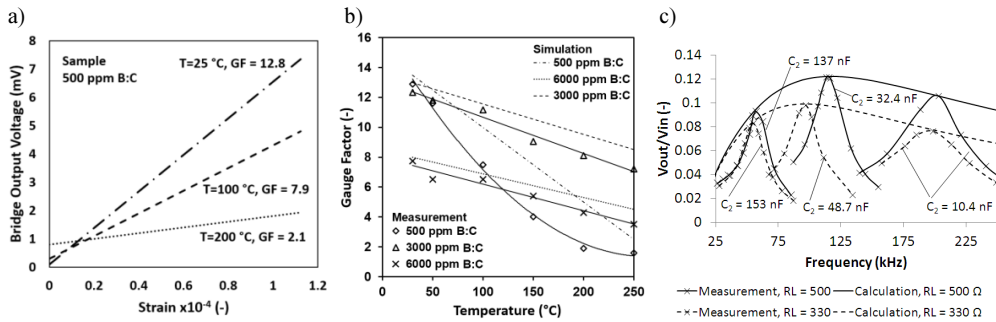


Fig. 6. a) The set of curves representing strain dependences of a strain gauge bridge output voltage for samples with lowest dopant level 500 ppm B:C (when the bridge bias of 5 V was applied) at different ambient temperatures T (25°C to 200°C); b) temperature dependency of *GF* for different doping levels and comparison with simulation results; c) comparison of the voltage transfer calculation and measurement results of the voltage transfer for three resonance frequencies. Powering distance is 4 cm and secondary coil is placed over the metal plate in distance 13 mm ($L_1 = 28.6 \mu\text{H}$, $L_2 = 57.8 \mu\text{H}$, $R_{L2} = 3.5 \Omega$, $R_L = 500 \Omega$; 330Ω , $k = 0.014$, $V_0 \approx V_m = 1 \text{ V}$, $R_0 = R_{L1} = 0 \Omega$, $C_1 = 0 \text{ F}$, C_2 sets the circuit in the resonance).

The sensitivity of the sensor with the lowest dopant level rapidly decreases with increasing the temperature (see Fig. 6a). It is caused by the temperature-dependent strain *Gauge Sensitivity* (*GF* decreases from 12.8 (-) @ 25°C to 2 (-) @ 250°C), as shown in Fig. 6b. Samples with a higher doping level exhibit lower TCR and also the temperature dependency of *GF*. This is in a good agreement with the simulation results, where simulated values are more optimistic (up to 10% higher). The reason is that the MemPZR solver can simulate the temperature

dependence of conductivity and piezo-resistive coefficient, but other effects on diamond grain boundaries (mainly at elevated temperatures) and an influence of the condition circuit are not taken into account. Simulations are precise enough for estimation of sensor parameters at lower temperatures.

4.2. Wireless powering

The theoretical calculations of the optimal operating frequency were verified – only small corrections of the resonance capacitors must be performed to compensate the device tolerances and parasitic properties of the coils.

Figure 6c presents comparison of the theoretical calculations and measurement results of the wireless powering between the coils from Table 1. The powering was applied for the axial distance of 4 cm and the secondary coil was placed on the large metal plate at the distance of 13 mm to simulate real conditions on the metal blade.

The measurement verified validity of the equations for the optimal resonance frequency and the optimal capacitor C_2 value (7), (8). The voltage transfer can be affected by the coupling coefficient change (see (9)), because it is a very distance-dependent parameter. This variation can be compensated by a sufficient margin of the excitation voltage.

The system proved its capability to transfer the power of 100 mW at the distance of 4 cm with the efficiency of 14%. The efficiency of the power transfer depends on the coil quality factor – particularly the L_1 coil losses are critical. The primary parallel resonance matching is also an important parameter and it is affected by the distance (coupling coefficient).

5. Wireless measuring probe

The results of theoretical calculations and simulations were tested on the real application. Fig. 7a presents a schematic of high-temperature evaluating circuit that can be used for the piezo-resistive strain sensor S1 from Chapter 2. It consists of high temperature operational HT1104 amplifiers which can be used in the temperature range $-55^\circ\text{C} \div +225^\circ\text{C}$. The powering voltage is rectified by the TS4148 diodes ($-65^\circ\text{C} \div +200^\circ\text{C}$). Other components in the schematic are passive and they are selected to withstand the high temperature.

The differential voltage signal from the strain sensor S1 is evaluated using the instrumentation amplifier (IC2A, IC2B and IC2D) and then compared with the triangular signal from the generator (IC1A, IC1B). At the output of IC1C comparator is a pulse-width modulated signal that can be sent to the transmitter [27].

As mentioned in Section 3, a crucial part of the powering strategy is finding the optimal operating frequency that is affected mainly by the coils' properties and by the expected loading impedance. The loading impedance can be found using the minimal powering voltage and the current consumption of the circuit. The minimal powering voltage for the HT1104 amplifiers is 5 V and the evaluating circuit consumes about 10 mA at this voltage. Thus, the loading resistor R_L value is equal to 500 Ω .

The coils used for powering and for communication are planar spiral coils, which differ from those discussed in Section 3.6. The character of the coupling coefficient differs from the curves in Fig. 5a, but the difference is not significant. The diameters of both coils are 15 cm and the maximal required distance for powering is 13 cm, where the coupling coefficient k is about 0.02. Using (7), (8), (9), the optimal operating frequency of 140 kHz can be calculated and the voltage transfer is equal to 0.34. Due to the voltage drop on the rectifying diodes the received voltage should be at least 7 V. Thus, the primary voltage V_0 must be at least 21 V and the capacitor C_1 value should be 240 nF.

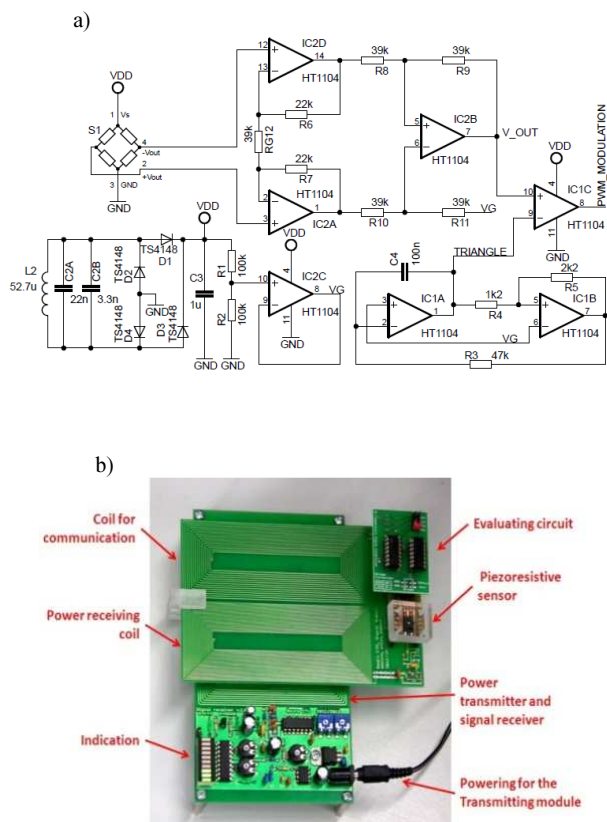


Fig. 7. a) A schematic of high-temperature measuring probe; b) the constructed test bench with the wireless powering and data transfer.

Figure 7b presents the test device for testing the wireless powering and the high-temperature evaluating circuits. The output signal from the piezo-resistive bridge sensor is amplified and it modulates the duty cycle of the output signal.

The measuring probe has two coils – the coil for powering and the coil for communication. The powering coil is set to the optimal resonance frequency to maximize the powering voltage transfer. The coil for communication is not loaded and thus the operating frequency is not critical. The communication frequency is set to 420 kHz. This frequency equals to the 3rd harmonic component of the square signal with the frequency of the powering coil. This concept simplifies the design of the excitation signal source. The coil for communication is in resonance and is switched to the modulating resistor by the output PWM signal from the measuring probe. The signal is detected on the primary side by sensing the input impedance change (a concept typical for passive RFID systems) and passed to the base station for further acquisition using a counter and displaying it on the bar LED indicator.

6. Conclusions

The paper presents a system which uses a novel strain sensor based on nano-crystalline layers suitable for harsh-environment applications and wireless powering using the near magnetic field. Unlike other types of wireless powering the near magnetic field enables the high power transfer and long-term operation. It withstands a harsh environment and preserves

the electromagnetic compatibility with a remote environment. The paper presents a solution for optimizing the operational frequency using the basic parameters of powering system. The principle was tested on a real application with components that were able to operate at up to 200°C. The presented system is highly modular and it can be easily adapted to measure other electrical or nonelectrical quantities, such as the pressure, temperature, light intensity, *etc.*

Acknowledgements

The research presented in the paper has been supported by the Czech Ministry of Interior research program No. VG20102015015 – “Miniature intelligent system for analysing concentrations of gases and pollutants, particularly toxic” (2010-2015, MV0/VG). Special thanks to A. Kromka (Institute of Physics of the Czech Academy of Sciences, Czech Republic) and K. Haenen (Hasselt University, Belgium) for preparation of samples with boron doped nano-crystalline diamond.

References

- [1] Werner, M.R., Fahrner, W.R. (2001). Review on Materials, Microsensors, Systems, and Devices for High-Temperature and Harsh-Environment Applications. *IEEE Transactions on Industrial Electronics*, 48(2), 249–257.
- [2] Ćwirko, J., Ćwirko, R., Mikołajczyk, J. (2015). Comparative Tests of Temperature Effects on the Performance of Gan and Sic Photodiodes. *Metrol. Meas. Syst.*, 22(1), 119–126.
- [3] Davis, L., Holmes, K., Davidson, J.L., Kang, W.P., Henderson, T.G., Eidson, R., Howell, M., Kerns, D.V. (1998). Diamond Microelectromechanical Sensors (DMEMS). *High Temperature Electronics Conference, HITEC*, 274–279.
- [4] Bogdanowicz, R. (2014). Characterization of Optical and Electrical Properties of Transparent Conductive Boron-Doped Diamond thin Films Grown on Fused Silica. *Metrol. Meas. Syst.*, 21(4), 685–698.
- [5] Kohn, E., Gluche, P., Adamschik, M. (1999). Diamond MEMS a new emerging technology. *Diam. Rel. Mater.*, 8, 934–940.
- [6] Dziurdzia, P., Mysiura, M., Gołda, A. (2012). Low Voltage Integrated Converter for Waste Heat Thermoelectric Harvesters. *Metrol. Meas. Syst.*, 19(1), 159–168.
- [7] Janeczka, K., Jakubowska, M., Kozioł, G., Jankowski-Miśkiewicz, P. (2013). Passive UHF RFID-Enabled Sensor System For Detection Of Product’S Exposure To Elevated Temperature. *Metrol. Meas. Syst.*, 20(4), 591–600.
- [8] Francesca, T. (2012). Wireless Power Charging a unified set of industry objectives for Consumers. *powerbyproxi.com*
- [9] Linear Technology Corporation. (2013). FAQs: Wireless Power Transfer (WPT) & LTC4120, www.linear.com/docs/44012 (Mar. 2014).
- [10] LTC4120 – Wireless Power Receiver and 400 mA Buck Battery Charger. Datasheet for Linear Technology Corporation, <http://www.linear.com/docs/43861> (Mar. 2014).
- [11] Jaegue, S., Seungyong, S., Yangsu, K., Seungyoung, A., Seokhwan, L., Guho, J., Seong-Jeub, J., Dong-Ho, Ch. (2014). Design and Implementation of Shaped Magnetic-Resonance-Based Wireless Power Transfer System for Roadway-Powered Moving Electric Vehicles. *Industrial Electronics IEEE Transactions on*, 61(3), 1179–1192.
- [12] Dukju, A., Songcheol, H. (2014). Wireless Power Transmission With Self-Regulated Output Voltage for Biomedical Implant. *IEEE Transactions on Industrial Electronics*, 61(5), 2225–2235.
- [13] Lawson, C.P., Ivey, P.C. (2005). Turbomachinery blade vibration amplitude measurement through tip timing with capacitance tip clearance probes. *Sensors and Actuators A: Physical*, 118(1), 14–24.
- [14] Procházka, P., Vaněk, F. (2014). New Methods of Noncontact Sensing of Blade Vibrations and Deflections in Turbomachinery. *IEEE Transactions on Instrumentation and Measurement*, 63(6), 1583–1592.

- [15] Dreier, F., Günther, P., Pfister, T., Czarske, J. W., Fischer, A. (2013). Interferometric sensor system for blade vibrations measurements in turbomachine applications. *IEEE Trans. Instrum. Meas.*, 62(8), 2297–2302.
- [16] Arsenault, T.J., Achuthan, A., Marzocca, P., Grappasonni, C., Coppotelli, G. (2013). Development of a FBG based distributed strain sensor system for wind turbine structural health monitoring. *Smart Mater. Struct.*, 22, 075027, 1–11.
- [17] Abdelrhman, A.M., Hee, L.M., Leong, M.S. (2014). Condition Monitoring of Blade in Turbomachinery: A Review. *Advances in Mechanical Engineering*, 2014.
- [18] Kumar, S., Roy, N., Ganguli, R. (2007). Monitoring low cycle fatigue damage in turbine blade using vibration characteristics. *Mechanical Systems and Signal Processing*, 21(1), 480–501.
- [19] Aslam, M., Taher, I., Masood, A., Tamor, M.A., Potter, T.J. (1992). Piezoresistivity in Vapor-Deposited Diamond Films. *Applied Physics Letters*, 60, 2923–2925.
- [20] Sahli, S., Aslam, D.M. (1998). Ultra-high sensitivity intra-grain poly-diamond piezoresistors. *Sensors and Actuators a-Physical*, 71, 193–197.
- [21] Janssens, S.D., Drijkoningen, S., Haenen, K. (2014). Large piezoresistive effect in surface conductive nanocrystalline diamond. *Appl. Phys. Lett.*, 105, 101601.
- [22] Dorsch, O., Holzner, K., Werner, M., Obermeier, E., Harper, R.E., Johnston, C., Chalker, P.R., Buckley-Golder, I. M. (1993). Piezoresistive Effect of Boron-Doped Diamond Thin-Films. *Diamond and Related Materials*. 2, 1096–1099.
- [23] Gajewski, W., Achatz, P., Williams, O.A., Haenen, K., Bustarret, E., Stutzmann, M., Garrido, J.A. (2009). Electronic and optical properties of boron-doped nanocrystalline diamond films. *Physical Review B*, 79(4), 045206.
- [24] Kulha, P., Kromka, A., Babchenko, O., Husak, M., Haenen, K. (2012). Design And Fabrication Of Piezoresistive Strain Gauges Based On Nanocrystalline Diamond Layers. *Vacuum*, 86(6), 757–760.
- [25] Chen, L., Liu, S., Zhou, Y. Ch., Cui, T.J. (2013). An Optimizable Circuit Structure for High-Efficiency Wireless Power Transfer. *IEEE Transactions on Industrial Electronics*, 60(1), 339–349.
- [26] Bouřa, A., Husák, M. (2012). Communication and Powering Scheme for Wireless and Battery-Less Measurement. *Radioengineering*, 21(1/II), 239–245.
- [27] Bouřa, A., Kulha, P., Husák, M. (2009). Simple Wireless A/D Converter for Isolated Systems. *IEEE ISIE 2009, IEEE International Symposium on Industrial Electronics*, Wonmi-gu, Gyeonggi-do: Institute of Control, Robotics and Systems (ICROS), 323–328.